

Fractal plasmonic metamaterials for subwavelength imaging

Xueqin Huang,¹ Shiyi Xiao,¹ Dexin Ye,² Jiangtao Huangfu,²
Zhiyu Wang,² Lixin Ran,² and Lei Zhou^{1,*}

¹Surface Physics Laboratory (State Key Laboratory) and Physics Department,
Fudan University, Shanghai 200433, P. R. China

²The Electromagnetic Academy at Zhejiang University, Zhejiang University,
Hangzhou 310027, P. R. China

*phzhou@fudan.edu.cn

Abstract: We show that a metallic plate with periodic fractal-shaped slits can be homogenized as a plasmonic metamaterial with plasmon frequency dictated by the fractal geometry. Owing to the *all-dimensional subwavelength* nature of the fractal pattern, our system supports both transverse-electric and transverse-magnetic surface plasmons. As a result, this structure can be employed to focus light sources with *all-dimensional subwavelength* resolution and enhanced field strengths. Microwave experiments reveal that the best achievable resolution is only $\lambda/15$, and finite-difference-time-domain simulations demonstrate that similar effects can be realized at infrared frequencies with appropriate designs.

©2010 Optical Society of America

OCIS codes: (100.6640) Superresolution; (160.3918) Metamaterials; (240.6680) Surface plasmons.

References and links

1. T. W. Ebbesen, H. J. Lezec, H. F. Ghaemi, T. Thio, and P. A. Wolff, "Extraordinary optical transmission through sub-wavelength hole arrays," *Nature* **391**(6668), 667–669 (1998).
2. J. A. Porto, F. J. Garcia-Vidal, and J. B. Pendry, "Transmission resonances on metallic gratings with very narrow slits," *Phys. Rev. Lett.* **83**(14), 2845–2848 (1999).
3. H. J. Lezec, A. Degiron, E. Devaux, R. A. Linke, L. Martin-Moreno, F. J. Garcia-Vidal, and T. W. Ebbesen, "Beaming light from a subwavelength aperture," *Science* **297**(5582), 820–822 (2002).
4. W. L. Barnes, A. Dereux, and T. W. Ebbesen, "Surface plasmon subwavelength optics," *Nature* **424**(6950), 824–830 (2003).
5. E. Ozbay, "Plasmonics: merging photonics and electronics at nanoscale dimensions," *Science* **311**(5758), 189–193 (2006).
6. J. M. Pitarke, V. M. Silkin, E. V. Chulkov, and P. M. Echenique, "Theory of surface plasmons and surface-plasmon polaritons," *Rep. Prog. Phys.* **70**(1), 1–87 (2007).
7. J. Gomez Rivas, C. Schotsch, P. Haring Bolivar, and H. Kurz, "Enhanced transmission of THz radiation through subwavelength holes," *Phys. Rev. B* **68**(20), 201306 (2003).
8. W. Cai, D. A. Genov, and V. M. Shalaev, "Superlens based on metal-dielectric composites," *Phys. Rev. B* **72**(19), 193101 (2005).
9. X. Yang, Y. Liu, J. Ma, J. Cui, H. Xing, W. Wang, C. Wang, and X. Luo, "Broadband super-resolution imaging by a superlens with unmatched dielectric medium," *Opt. Express* **16**(24), 19686–19694 (2008).
10. R. A. Shelby, D. R. Smith, and S. Schultz, "Experimental verification of a negative index of refraction," *Science* **292**(5514), 77–79 (2001).
11. T. J. Yen, W. J. Padilla, N. Fang, D. C. Vier, D. R. Smith, J. B. Pendry, D. N. Basov, and X. Zhang, "Terahertz magnetic response from artificial materials," *Science* **303**(5663), 1494–1496 (2004).
12. F. J. Garcia-Vidal, L. Martin-Moreno, and J. B. Pendry, "Surfaces with holes in them: new plasmonic metamaterials," *J. Opt. A, Pure Appl. Opt.* **7**(2), S97–S101 (2005).
13. J. B. Pendry, L. Martin-Moreno, and F. J. Garcia-Vidal, "Mimicking surface plasmons with structured surfaces," *Science* **305**(5685), 847–848 (2004).
14. J. Jung, F. J. Garcia-Vidal, L. Martin-Moreno, and J. B. Pendry, "Holey metal films make perfect endoscopes," *Phys. Rev. B* **79**(15), 153407 (2009).
15. Y. M. Shin, J. K. So, K. H. Jang, J. H. Won, A. Srivastava, and G. S. Park, "Evanescent tunneling of an effective surface plasmon excited by convection electrons," *Phys. Rev. Lett.* **99**(14), 147402 (2007).

16. C. Puente-Baliarda, J. Romeu, R. Pous, and A. Cardama, "On the behavior of the Sierpinski multiband fractal antenna," *IEEE Trans. Antenn. Propag.* **46**(4), 517–524 (1998).
17. K. J. Vinoy, K. A. Jose, V. K. Varadan, and V. V. Varadan, "Hilbert curve fractal antenna: a small resonant antenna for VHF/UHF applications," *Microw. Opt. Technol. Lett.* **29**(4), 215–219 (2001).
18. D. H. Werner and S. Ganguly, "An overview of fractal antenna engineering research," *IEEE Antenn. Propag. Mag.* **45**(1), 38–57 (2003).
19. W. Wen, Z. Yang, G. Xu, Y. Chen, L. Zhou, W. Ge, C. T. Chan, and P. Sheng, "Infrared passbands from fractal slit patterns on a metal plate," *Appl. Phys. Lett.* **83**(11), 2106–2108 (2003).
20. W. Wen, L. Zhou, B. Hou, C. T. Chan, and P. Sheng, "Resonant transmission of microwaves through subwavelength fractal slits in a metallic plate," *Phys. Rev. B* **72**(15), 153406 (2005).
21. F. Miyamaru, Y. Saito, M. W. Takeda, B. Hou, L. Liu, W. Wen, and P. Sheng, "Terahertz electric response of fractal metamaterial structures," *Phys. Rev. B* **77**(4), 045124 (2008).
22. A. Ono, J. Kato, and S. Kawata, "Subwavelength optical imaging through a metallic nanorod array," *Phys. Rev. Lett.* **95**(26), 267407 (2005).
23. P. A. Belov, Y. Hao, and S. Sudhakaran, "Subwavelength microwave imaging using an array of parallel conducting wires as a lens," *Phys. Rev. B* **73**(3), 033108 (2006).
24. X. Li, S. He, and Y. Jin, "Subwavelength focusing with a multilayered Fabry-Perot structure at optical frequencies," *Phys. Rev. B* **75**(4), 045103 (2007).
25. S. Maslovski, S. Tretyakov, and P. Alitalo, "Near-field enhancement and imaging in double planar polariton-resonant structures," *J. Appl. Phys.* **96**(3), 1293–1300 (2004).
26. P. Alitalo, C. Simovski, A. Viitanen, and S. Tretyakov, "Near-field enhancement and subwavelength imaging in the optical region using a pair of two-dimensional arrays of metal nanospheres," *Phys. Rev. B* **74**(23), 235425 (2006).
27. C. Mateo-Segura, C. R. Simovski, G. Goussetis, and S. Tretyakov, "Subwavelength resolution for horizontal and vertical polarization by coupled arrays of oblate nanoellipsoids," *Opt. Lett.* **34**(15), 2333–2335 (2009).
28. I. El-Kady, M. M. Sigalas, R. Biswas, K. M. Ho, and C. M. Soukoulis, "Metallic photonic crystals at optical wavelengths," *Phys. Rev. B* **62**(23), 15299–15302 (2000).
29. Free FDTD package MIT Electromagnetic Equation Propagation (MEEP). To calculate the SPP band structures, we put an *x*-polarized point source as an excitation in a plane just above the structure, at a position deviating slightly from the center. One unit cell was used as the computation domain with periodic boundary conditions imposed, and the mesh size was taken as $0.02 \times 0.02 \times 0.02 \mu\text{m}$. Convergences of the calculations were carefully examined.
30. In the frequency domain of interest in this work (e.g., from microwave to infra-red), the SPP characteristics of the designed system are mainly determined by the geometry of the structure, rather than the dielectric properties of the constitutional material that we used. However, at higher frequencies (e.g. visible), material loss and dispersions play more important roles.
31. H. Raether, *Surface Plasmons (ed. G. Hohler)* (Springer, Berlin, 1988).
32. J. B. Pendry, "Negative refraction makes a perfect lens," *Phys. Rev. Lett.* **85**(18), 3966–3969 (2000).
33. N. Fang, H. Lee, C. Sun, and X. Zhang, "Sub-diffraction-limited optical imaging with a silver superlens," *Science* **308**(5721), 534–537 (2005).
34. A drawback of our lens is that it only works for sources with definite in-plane electric polarization. This problem can be remedied by replacing the fractal shape by some isotropic patterns.
35. In our experiments, we only measured the one-dimensional field distributions along the line perpendicular to the antenna on the image planes.
36. CONCERTO 7.0, Vector Fields Limited, England, (2008). The basic mesh size was taken as $0.5 \times 0.5 \times 1 \text{mm}$ for microwave calculations, and $0.02 \times 0.02 \times 0.02 \mu\text{m}$ for infrared calculations, and finer meshes were adopted in the regions wherever necessary. Convergences of the calculations were carefully examined.
37. Here, the experimentally measured field enhancement is not obvious (about 2 times comparing with the air case). This is because the source dipole antenna adopted in experiment is too long so that the efficiency of coupling with SPP is relatively low. In addition, since the receiver antenna is also too long, the received signal actually represents an averaged field over the area covered by the antenna, and therefore, the strong local field enhancement is smeared.
38. FDTD simulations revealed that similar behaviors exist when we shift the source along *y* direction inside a unit cell, and the formed image consists of two peaks when the source is right at the *y*-direction boundary of two adjacent unit cells.
39. L. Zhou, and C. T. Chan, "Relaxation mechanisms in three-dimensional metamaterial lens focusing," *Opt. Lett.* **30**(14), 1812–1814 (2005).
40. The transmittance cannot reach 1 due to the material losses.

1. Introduction

Surface plasmon polaritons (SPPs) are elementary electromagnetic (EM) excitations bounded at metal/dielectric interfaces, and attracted considerable attention recently [1–6]. For a natural material, its plasmon frequency (ω_p) is fixed by the electron density. It has been shown that

ω_p can be modified via using semiconductors [7] or metal/dielectric composites [8,9] at the optical/infrared frequency range, but the ideas are difficult to extend to microwave frequencies where metals are nearly perfect electric conductors. Recently, people showed that Bragg scatterings can modulate the SPPs significantly, and found high optical transmissions in a silver film drilled with periodic holes [1–3]. However, the Bragg mechanism can only fold the SPP bands into the first Brillouin zone, but cannot change ω_p of a material. Although metamaterials [10,11] can in principle possess any desired EM wave properties at arbitrary frequencies, the fabrications of high-quality metamaterials are still challenging. In 2004, Pendry *et al.* demonstrated that a metallic plate with periodic square holes can mimic a plasmonic metamaterial in terms of SPP properties, with effective ω_p being the waveguide cut-off frequency of the hole [12,13]. This opens up a way to design artificial plasmonic metamaterials at any desired frequencies, and Jung *et al.* recently suggested employ such materials to make perfect endoscopes [14]. However, to make the idea work, one has to fill the holes with *high-index materials* to make the cut-off wavelength much longer than the periodicity [12,13]. The high-index material is not easy to realize in practice, particularly at higher frequencies. Very recently, Shin *et al.* [15] showed that high-index insertion is not necessary if the square holes are replaced by closely packed narrow rectangular holes with cross sections $b_x \times b_y$ ($b_x \ll b_y$). Indeed, such a hole has a cut-off wavelength $\lambda = 2b_y$ much longer than the periodicity along x direction ($\sim b_x$ since the holes are closely packed) [15]. However, since such holes are subwavelength *only* along *one* direction, we will show that the generated SPPs on such structures *only* have transverse-magnetic (TM) polarization travelling along *one* direction. This limitation restricts the applications of such structures in some cases.

Attracted by the multiband and subwavelength properties of fractals, several groups investigated the rich EM wave characteristics of various fractal structures [16–21]. Inspired by these prior works, here we study a metallic plate drilled with fractal-shaped slits, and demonstrate that the system exhibits SPPs with ω_p dictated by the fractal geometry. Without using high-index insertions [12,13] and distinct from the narrow rectangular hole case [15], here the fractal pattern is *subwavelength along all dimensions* at resonance. Therefore, we find such a system can be homogenized as a plasmonic metamaterial to support TM and transverse-electric (TE) polarized SPPs *simultaneously*. We further show by both experiments and finite-difference-time-domain (FDTD) simulations that our structure works as a near-field *super* lens to focus light sources with *all dimensional subwavelength* resolution (best achievable resolution $\sim \lambda/15$), with physical mechanism different from other lenses discussed previously [22–27].

2. SPP band structures

Figure 1 schematically shows our structure — a $0.5\mu\text{m}$ -thick silver film caved with 4-level fractal slits arranged periodically with a lattice constant $a = 1\mu\text{m}$. Here, we chose this particular H-shaped fractal pattern because it has superior multiband and subwavelength responses, as shown in previous studies [19–21]. However, although the EM wave transmission properties of similar structures had been studied previously in different frequency domains [19–21], the *SPP characteristics* of such structures have never been addressed before and are the topics of the present work.

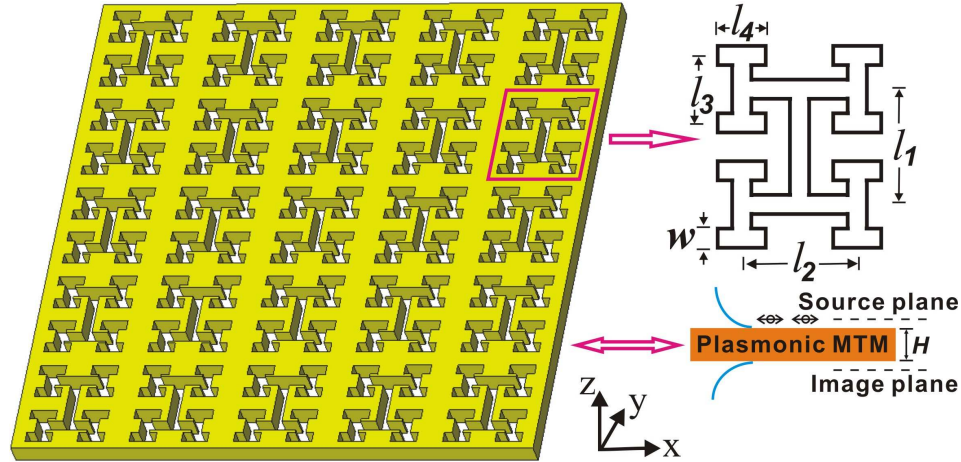


Fig. 1. Geometry of the fractal plasmonic metamaterial (MTM). Unit cell structure:
 $l_1 = l_2 = 0.5\mu\text{m}$, $l_3 = l_4 = 0.25\mu\text{m}$, $w = 0.06\mu\text{m}$, $H = 0.5\mu\text{m}$.

Taking the dielectric constant of silver as $\epsilon_{Ag} = 5 - f_p^2 / f(f + if_\gamma)$ with $f_p = 2175\text{THz}$ and $f_\gamma = 4.35\text{THz}$ [28], we performed FDTD simulations [29] to calculate the SPP band structure of the designed system [30]. Since this system shows no x - y symmetry, we depicted in Figs. 2(a) and 2(b) the SPP bands along $\Gamma \rightarrow X$ and $\Gamma \rightarrow X'$ directions, respectively, with $X = [\pi/a, 0, 0]$, $X' = [0, \pi/a, 0]$. In each panel, we found two SPP bands well below the light lines (solid pink line), which bend drastically as approaching at two frequencies ($f_{p1} = 41\text{THz}$, $f_{p2} = 78.7\text{THz}$, denoted by two dashed lines). We employed the attenuated total reflection technique to identify the polarization properties of the SPP bands. With k_x fixed as π/a , we shine evanescent waves with different polarizations on the structure, and depicted in Fig. 2(c) the transmission spectra for $\vec{E} \parallel \hat{x}$ (red circles) and $\vec{E} \parallel \hat{y}$ (blue line) polarizations. By comparing Figs. 2(a) with 2(c), we found that the lower SPP band in Fig. 2(a) is apparently TM-like, since a TM-polarized evanescent wave can excite this mode but a TE one cannot. Similarly, we identified polarizations of all SPP bands and then label them correspondingly on the figure. This is intriguing at first sight, since a complex structure at resonance usually exhibits complicated local field distribution, making it impossible to identify the eigenmode polarizations. We can understand these TE-like and TM-like SPPs in the spirit of “metamaterial”. As the probing wavelength is much longer than the unit-cell size, one can perform field average to homogenize the complex structure as an effective medium. Thanks to the high symmetry of the fractal geometry, the averaged field exhibits well-defined polarization characteristic so that identifying the SPP mode polarization becomes possible. The above discussions also revealed that, other symmetric and subwavelength patterns can be carefully designed to replace the H-shaped fractal to realize similar effects.

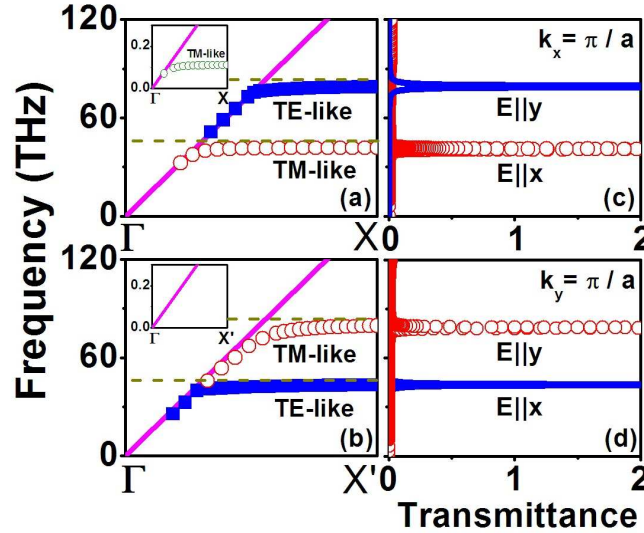


Fig. 2. SPP band structures of the fractal plate calculated by FDTD simulations for (a) $\Gamma \rightarrow X$ and (b) $\Gamma \rightarrow X'$ directions; Under the conditions of (c) $k_x = \pi/a$ and (d) $k_y = \pi/a$, FDTD calculated transmission spectra under incident plane evanescent waves with different polarizations. Insets: SPP band structures of rectangle hole plate calculated by FDTD simulations, with structural details $d = 1\mu\text{m}$, $s = 4.2d$, $a = 0.3d$, $L = 0.5d$ (see Ref. [15]).

The crucial advantage of our structure is clear. Whereas a flat Ag film supports only TM polarized SPP [31], our system supports *simultaneously* TM-like and TE-like SPPs related to each resonance. We also studied a metal plate with narrow rectangular holes [15], and depicted its SPP dispersions in the insets to Figs. 2(a)-2(b). Indeed, this structure exhibits an SPP band even without high-index insertions. However, in sharp contrast to our case, such a system supports only a single TM-like SPP band traveling along x direction [inset to Fig. 2(a)]. This is because the rectangle shape is subwavelength along only one (x) direction, and therefore, the SPP band along y direction *cannot* be formed since the subwavelength condition is not satisfied [12,13]. In contrast, our fractal pattern is *subwavelength* along *all directions* and possesses *multiple* resonances, so that for each resonance, SPP bands along both x and y directions can be formed (see Fig. 2).

FDTD simulations show that the plasmon frequencies can be changed via adjusting the fractal geometry. Taking 3-level and 4-level fractals as examples, we show in Fig. 3 that the plasmon resonance wavelength λ_p of the material changes from $4\mu\text{m}$ to $10\mu\text{m}$ via only adjusting the line width w , with the periodicity fixed as $a = 1\mu\text{m}$. Only the wavelengths of the fundamental plasmonic modes are depicted in Fig. 3 as an illustration. The plasmon wavelength can be further changed to cover an ultra-wide range (from infrared to microwave) by scaling the unit size a from $1\mu\text{m}$ to 1cm [see the inset to Fig. 3]. Therefore, we can in principle design a plasmonic metamaterial at any desired frequency. In addition, we note that λ_p is *independent* of the sample thickness.

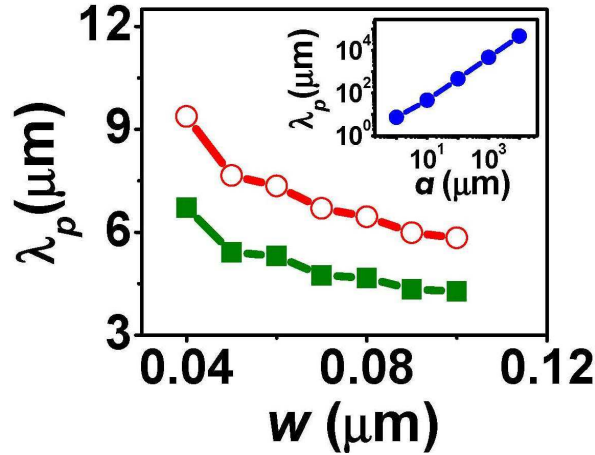


Fig. 3. FDTD calculated plasmon wavelength λ_p as functions of the slit width w when the fractal is 3-level (solid squares) and 4-level (open circles). Inset shows the calculated λ_p as a function of the periodicity a of the fractal array.

3. Subwavelength imaging

One can employ our structure to realize many SPP-based applications. It was shown both theoretically [32] and experimentally [33] that a silver film works as a lens to focus near field light sources with subwavelength resolution. However, such a *super* lens does not function at a frequency other than silver's natural SPP frequency, and since silver only supports TM-polarized SPPs, the source has to be carefully designed to emit p waves only [33]. In what follows, we show that our structure can collect both s and p waves emitted from a source to form an *all-dimensional subwavelength* image [34].

We first performed microwave experiments to demonstrate this idea. We designed a plasmonic metamaterial [picture given in Fig. 4(a)] with unit-cell shown schematically in the right panel of Fig. 4(a). Slightly different from an ideal fractal, the structure is purposely designed such that it is more compact in x direction. We then fabricated a series of samples with different thicknesses H . In our imaging experiments, we put a dipole antenna on the source plane 1mm above the lenses, and placed a receiver dipole antenna on an image plane 1mm below the lenses to measure the field distributions of the images [35]. Similar to other super lens imaging proposals [22–27,32,33], here the source is put very near to the lens. Both antennas are polarized along the y direction, connected to a vector network analyzer (Agilent 8722ES), and working at $f = 2.52\text{GHz}$ coinciding with the plasmon frequency of the designed lenses for y polarization [34]. When the source antenna is put at the unit-cell center, the images formed by two lenses with thicknesses $H = 31.5\text{mm}$, $H = 63\text{mm}$ are depicted in Figs. 4(b) and 4(c) as open circles, which are in excellent agreements with the corresponding FDTD simulations (solid lines) [36]. Both measurements and FDTD results show that the images focused by our lenses are only $\sim 8\text{mm}$ wide, which are $\sim \lambda / 15$ recalling $\lambda \approx 119\text{mm}$. In contrast, the images formed without lenses (solid squares) do *not* show any subwavelength resolutions at all. In addition, the field strength is enhanced when a lens is added [37]. The subwavelength resolution and enhanced field strength are two important characteristics of the SPP [4–6].

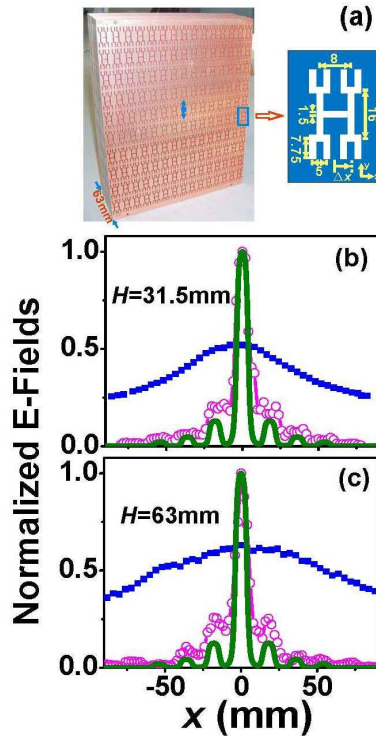


Fig. 4. (a). Picture of a 63mm-thick fractal plasmonic metamaterial and its unit cell structure (all lengths are measured in mm). Here the periodicity is 18mm (32mm) in x (y) direction. (b)-(c) Electric field distributions along the line perpendicular to the antenna on the image plane obtained by experiments (open circles) and FDTD simulations (solid lines) for different lens thickness, referenced by the experimental results measured without any lens (solid squares). Here, the maximum electric field is normalized to 1 in the presence of a lens.

In contrast to a flat silver-slab lens [32,33], our lens is not laterally homogeneous, and thus we need to test the position dependence of the imaging quality. Taking the $H = 63\text{mm}$ slab as a lens, we put the source at three typical positions inside one unit cell, labeled by Δx measuring the deviations from the center [see Fig. 4(a)], and then measured (calculated) the field patterns on the image plane. The patterns obtained experimentally and theoretically are shown in Fig. 5, correspondingly. When the source slightly deviates from the center, the field pattern [Fig. 5(a)] is essentially the same as the center case [Fig. 4(c)]. At a modest deviation $\Delta x = 7\text{mm}$, the image is still distinguishable with a sharp resolution, although a small peak arises caused by a neighboring unit cell. The image is totally undetectable only when the source is right at the unit-cell boundary, where two peaks of the same strength appear on the image plane [38]. Therefore, although the best resolution is $\sim \lambda/15$ achieved with the source put at the unit-cell center, the overall resolution is bounded by the periodicity a , which is $\sim \lambda/7$ in the present case. Indeed, we found experimentally that two sources placed within a distance larger than a are clearly distinguished on the image plane, while the same is *not* true without a lens.

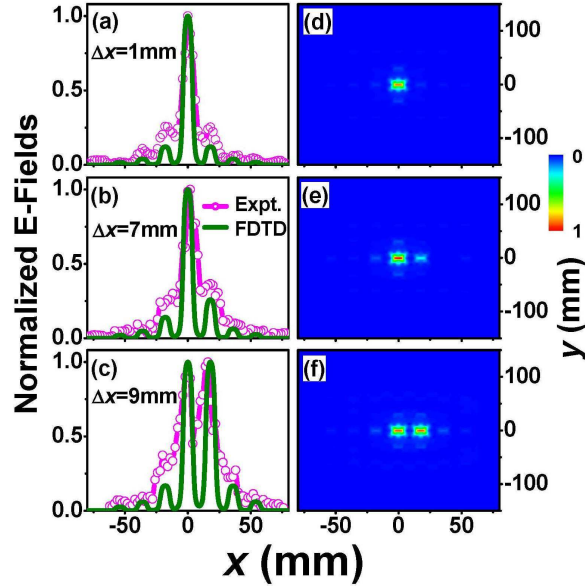


Fig. 5. Field distributions along the line perpendicular to the antenna on the image plane formed by the 63mm-thick lens when the source is placed at (a) $\Delta x = 1\text{mm}$, (b) $\Delta x = 7\text{mm}$, and (c) $\Delta x = 9\text{mm}$, obtained by measurements (open circles) and FDTD simulations (lines). Here the E field is normalized such that its maximum value is 1. The FDTD calculated two-dimensional patterns of the images for (d) $\Delta x = 1\text{mm}$, (e) $\Delta x = 7\text{mm}$, (f) $\Delta x = 9\text{mm}$.

Similar effects can be realized at infrared frequencies using the fractal structure designed for Fig. 2. As a comparison, we also adopted the rectangle-hole structure (same as that for Fig. 2) as a lens to focus light sources. We considered two types of source, i.e., two x -polarized dipoles working at 41 THz separated by $1\mu\text{m}$ either in x direction (case 1) or in y direction (case 2). For these two cases, we show the FDTD calculated images formed without any lenses in Figs. 6(a) and 6(d), those with a $0.5\mu\text{m}$ -thick rectangle-hole structure lens in Figs. 6(b) and 6(e), and those with our fractal structure lens in Figs. 6(c) and 6(f), correspondingly. Here, the source (image) plane is $0.1\mu\text{m}$ above (below) the lens [see the right panel in Fig. 1]. Since the sources are located within a subwavelength region (separation $1\mu\text{m} \ll \lambda = 7.3\mu\text{m}$), the two sources cannot be clearly distinguished without the lens [Fig. 6(a) and 6(d)]. With the rectangle-hole structure lens, case 1 can be distinguished [Fig. 6(b)] but the resolution along y direction is not subwavelength. More seriously, this lens cannot distinguish case 2 at all [Fig. 6(e)]. These are all caused by the fact that this structure does not support TE-polarized SPPs (see Fig. 2). With our lens, however, two sources are clearly distinguishable in both cases, and the formed images are *subwavelength along all directions*, with much enhanced field strength (see the E-field scales in Fig. 6). We also checked the imaging properties of two y -polarized dipole sources, and found similar behaviors if the working frequency is taken as 78.7 THz, coinciding with the plasmonic resonance of the fractal lens for y polarization (see Fig. 2).

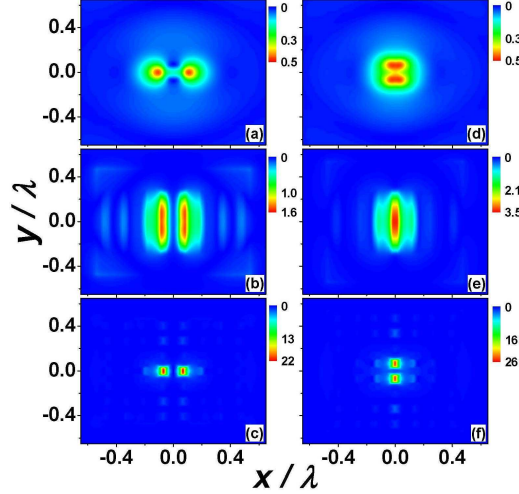


Fig. 6. FDTD calculated E-field patterns on the image planes obtained without a lens (a) + (d), with a rectangle-hole structure lens (b) + (e), and with our fractal structure lens (c) + (f). Here, the two x -polarized dipole sources are separated by $1\mu m$ in x direction for (a), (b), and (c), and in y direction for (d), (e) and (f). Both the rectangle-hole structure and fractal structure are the same as those in Fig. 2.

4. Physical mechanism

We now explore the underlying physics of the super imaging effect. Assume the source taking a simplest form $\vec{J}(\vec{r}, t) = \hat{x}P_0\delta(\vec{r})e^{-i\omega t}$, we can formally obtain the entire EM fields distributions by using a dyadic Green's function method [39]. Specifically, the x component of E-field on the image plane is found as

$$E_x(x, y) = -\frac{i\mu_0 P_0}{8\pi^2} \int \frac{e^{ik_{\parallel}(x\cos\phi + y\sin\phi)} e^{-ik_z d}}{k_z} \left[T^{TE}(k_{\parallel}) \sin^2 \phi + \frac{k_z^2}{k_0^2} T^{TM}(k_{\parallel}) \cos^2 \phi \right] k_{\parallel} dk_{\parallel} d\phi \quad (1)$$

where $k_z = \sqrt{k_0^2 - k_{\parallel}^2}$ with $k_0 = \omega/c$, d is the source-image distance, and $T^{TE}(k_{\parallel})$ and $T^{TM}(k_{\parallel})$ are the transfer functions for TE and TM waves (with $\vec{k} = k_z \hat{z} + \vec{k}_{\parallel}$) passing through the fractal structure. The field distributions, and in turn the image properties, can be understood once the transfer functions are known.

We have employed the FDTD method [36] to study the properties of the transfer functions $[T^{TE}(k_{\parallel}), T^{TM}(k_{\parallel})]$ for the designed fractal lens. For propagating components (i.e., $k_{\parallel} < k_0$), we found through FDTD simulations that the fractal structure supports high transmissions $T(k_{\parallel}) \approx 1$ at the working frequency [40]. More importantly, there is nearly *no phase change* for the transmitted waves under all incident angles and polarizations, as shown in Fig. 7 by open stars. Therefore, the information of all propagating components can be well transmitted through the fractal lens, without any distortions. In contrast, when the fractal lens is replaced by air, the phase change of transmitted wave strongly depends on the incidence angle, as shown in Fig. 7 by solid circles.

Let us consider the evanescent components radiated from the source (i.e., $k_{\parallel} > k_0$). To get an *all-dimensional subwavelength* resolution for the image, we need to collect the evanescent components for both TE and TM polarizations. Fortunately, our lens possesses flat SPP bands near the working frequency [see Figs. 2(a)-2(b)] for both TE and TM polarizations, so that those

evanescent components with $k_0 < k_{\parallel} < G$ can be transmitted across the lens, aided by such SPPs. Here, G is the reciprocal k vector of the lattice. To prove this point, we employed FDTD simulations to calculate the stabilized electric field distribution under a TM-polarized incident evanescent wave (with $\vec{H} \parallel \hat{y}$, $k_x = \pi/2a > k_0$), and depicted in Fig. 8(a) the field component E_x as a function of z on the line perpendicular to the fractal lens. To suppress the strong field fluctuations on xy -plane introduced by the complex microstructures, we have averaged E_x on xy -plane over a unit cell area, in the same spirit of “metamaterial”. While the field distributions in both sides of the lens (air regions) can be well fitted by exponential forms ($\sim e^{-\alpha z}$ with $\alpha = \sqrt{k_x^2 - k_0^2}$), we note from Fig. 8(a) that the field amplitude *keeps constant* inside the lens, indicating that the transfer function of evanescent component is nearly 1 (i.e., $T^{TM}(k_{\parallel}) \approx 1$). This conclusion is actually independent of k_{\parallel} and polarization, as shown in Fig. 8(b) for a TE-polarized evanescent wave excitation (with $\vec{E} \parallel \hat{x}$, $k_y = \pi/a > k_0$). Therefore, the information of all evanescent components with $k_0 < k_{\parallel} < G$ can also be well transmitted through the lens, without any distortions.

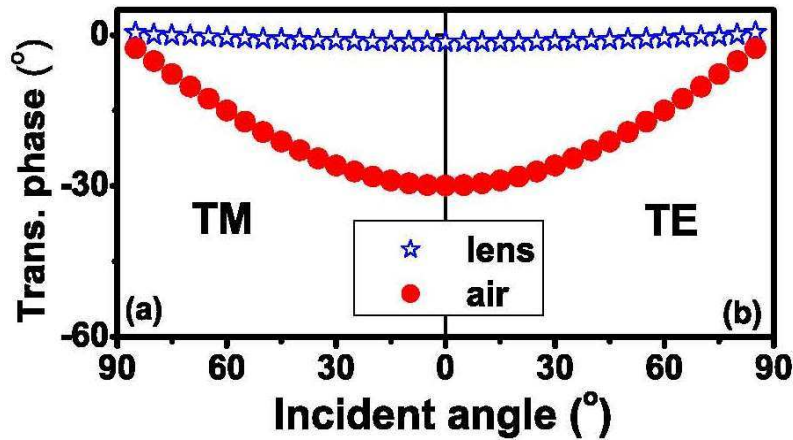


Fig. 7. FDTD calculated phase change of the transmitted wave through our fractal lens (blue stars) and an air layer of the same thickness (red circles) as functions of the incident angle for TM- (a) and TE-polarized (b) incident waves. Here, the working frequency is 41THz.

The mechanism of our super imaging effect is very clear. For a near field light source placed at the left side of the lens, both its propagating and evanescent components (with $k_0 < k_{\parallel} < G$) can be well transmitted through the lens without distortions, so that the image formed on the right side of the lens can beat the diffraction limit. However, since the maximum k vector of the SPP band is not infinity but G (see Fig. 2), there is a natural resolution limit for the image and the highest resolution is bounded by a – the unit cell size of our fractal structure. We note that a can be much less than the working wavelength λ_p , which is a property unique to the fractal geometry.

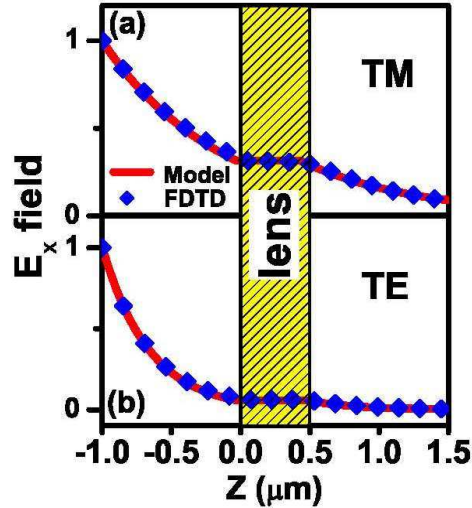


Fig. 8. Electric field distributions along the line perpendicular to the fractal structure for a TM-polarized incident evanescent wave with $k_x = \pi / (2a)$ (a) and a TE-polarized one with $k_y = \pi / a$ (b). Blue diamonds represent FDTD simulations while red lines represent appropriate fitting functions ($e^{-\alpha z}$ in air and straight lines in slab). Here, the working frequency is 41THz.

Our mechanism is different from many others [22–27]. In the mechanisms described in Refs [22–24], the operation frequencies were dictated by the lens thickness, since the resonance frequency is determined by the rod length in [22] and Fabry-Perot (FP) resonances were employed to reduce reflections in [23,24]. In contrast, our working frequency is *independent* of the lens thickness, demonstrated both experimentally and theoretically in Fig. 4. Compared to Refs [25–27], where a coupled pair of plasmonic material sheets was employed to realize subwavelength imaging, our device consists of only one plasmonic slab. However, previous discussions also revealed that our lens is essentially a near-field lens. In order to collect the evanescent waves efficiently, the source and image plane should be put close to the lens, which is a drawback compared with some other super lens proposals [24].

5. Conclusions

In conclusions, we showed that a metal plate with fractal-shaped slits can be viewed as a plasmonic metamaterial to support SPPs in both TE-like and TM-like polarizations, without using high-index insertions. We demonstrated by both FDTD simulations and microwave experiments that our structure can focus light sources with *all dimensional subwavelength* resolution at desired frequencies with careful designs.

Acknowledgments

This work was supported by the National Natural Science Foundation of China (60725417, 60990321, 60531020, 60671003, 60701007), NCET-07-0750, and Shanghai Science and Technology Committee (No. 08dj1400302).